Integrated magnetotelluric and petrological analysis of felsic magma reservoirs: Insights from Ethiopian rift volcanoes

Friedemann Samrock[a,*], Alexander V. Grayver[a], Olivier Bachmann[b], Özge Karakas[b], Martin O. Saar[a,c]

[a]ETH Zurich, Department of Earth Sciences, Institute of Geophysics, Zurich, Switzerland
[b]ETH Zurich, Department of Earth Sciences, Institute of Geochemistry and Petrology, Zurich, Switzerland
[c]University of Minnesota, Department of Earth and Environmental Sciences, Minneapolis, USA

*Corresponding author
Email address: fsamrock@ethz.ch (Friedemann Samrock)

Integrated magnetotelluric and petrological analysis of felsic magma reservoirs: Insights from Ethiopian rift volcanoes

Friedemann Samrock[a,*], Alexander V. Grayver[a], Olivier Bachmann[b], Özge Karakas[b], Martin O. Saar[a,c]

[a] *ETH Zurich, Department of Earth Sciences, Institute of Geophysics, Zurich, Switzerland*
[b] *ETH Zurich, Department of Earth Sciences, Institute of Geochemistry and Petrology, Zurich, Switzerland*
[c] *University of Minnesota, Department of Earth and Environmental Sciences, Minneapolis, USA*

Abstract

Geophysical and petrological probes are key to understanding the structure and the thermochemical state of active magmatic systems. Recent advances in laboratory analyses, field investigations and numerical methods have allowed increasingly complex data-constraint models with new insights into magma plumbing systems and melt evolution. However, there is still a need for methods to quantitatively link geophysical and petrological observables for a more consistent description of magmatic processes at both micro- and macro-scales. Whilst modern geophysical studies provide detailed 3-D subsurface images that help to characterize magma reservoirs by relating state variables with physical material properties, constraints from on-site petrological analyses and thermodynamic modelling of melt evolution are at best incorporated qualitatively.

Here, we combine modelling of phase equilibria in cooling magma and laboratory measurements of electrical properties of melt to derive the evolution of electrical conductivity in a crystallizing silicic magmatic system. We apply this framework to 3-D electrical conductivity images from magnetotelluric studies of two volcanoes in the Ethiopian Rift. The presented approach enables us to constrain

---

[*] Corresponding author
Email address: `fsamrock@ethz.ch` (Friedemann Samrock)

Preprint submitted to Earth and Planetary Science Letters *December 3, 2020*

key variables such as melt content, temperature and magmatic volatile abundance at depth. Our study shows that accounting for magmatic volatiles as an independent phase is crucial for understanding electrical conductivity structures in magma reservoirs at an advanced state of crystallization. Furthermore, our results deepen the understanding of the mechanisms behind volcanic unrest and help assess the long-term potential of hydrothermal reservoirs for geothermal energy production.

Keywords: magnetotelluric imaging, petrology, geochemistry, melt evolution, magmatic volatiles, volcano monitoring

---

1. Introduction

Our knowledge of volcanic systems, or more generally, magmatic processes, is built upon observations made across a variety of disciplines, including geology, geochemistry, petrology and geophysics. A major outstanding problem in volcanic studies is to characterize the current thermochemical state and constrain the spatial extent of a magmatic plumbing system (Bachmann & Huber, 2016; Cashman et al., 2017). In this study, we present a new combined geophysical-petrological framework for addressing this scientific challenge. The geophysical basis of our analysis are 3-D subsurface electrical conductivity images from active volcanic regions.

The approach is structured in four stages: First, we use Rhyolite-MELTS (Gualda et al., 2012) to reproduce the melt evolution and the composition of volcanic samples collected on the studied volcanoes. Second, we derive a generalized formulation based on laboratory-based melt electrical conductivity models to calculate the electrical conductivity, σ_{melt}, of the residual melt with varying degree of crystallization (Guo et al., 2016, 2017; Laumonier et al., 2019). Third, we use a mixing law that accounts for three phases (Glover, 2010), solid crystalline, liquid melt and free magmatic volatiles, to calculate the bulk electrical conductivity, σ_{bulk}, of the modelled magmatic system. Finally, we compare electrical conductivities from magnetotelluric field studies against σ_{bulk} to infer the current thermochemical state of the imaged magmatic systems.

Our study area is located in the Central Main Ethiopian Rift (CMER, Fig. 1), a present-day prime example of tectono-magmatic continental rifting. Quaternary to recent volcanoes in the CMER are emplaced along an in-rift extensional fault-system, known as the Wonji Fault Belt (WFB). The WFB forms a roughly N12°E striking right-stepping fault network, which acts as present-day center of magma ascent and extension with spreading rates of up to $6-7\,\mathrm{mm/yr}$ (Corti, 2009). Magmatism along the WFB shows a bimodal character with a predominance of silicic over basaltic products and a lack of intermediate volcanic rock (e.g. Rooney et al., 2007, and references therein). A number of geochemical-petrological studies in the CMER provide key information on how magma is formed and how its composition changes due to mixing, crustal assimilation and fractionation as it rises to the surface. Petrological studies suggest a well-developed two-level magmatic plumbing system under the WFB with a first

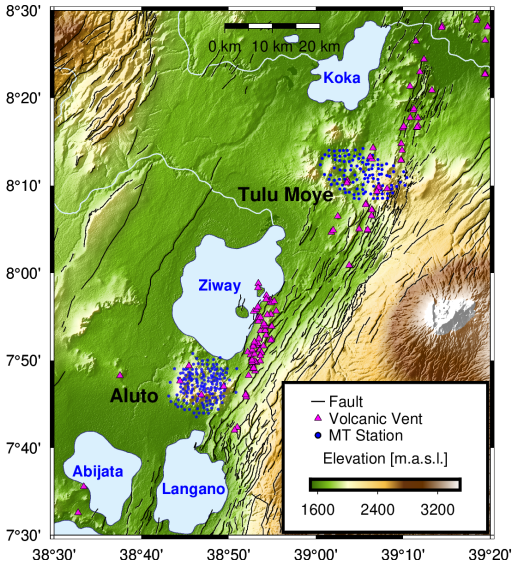

Figure 1: Overview map of the Central Main Ethiopian Rift (CMER) showing the Tulu Moye and Aluto study areas and the location of volcanic vents along the N12°E striking fault network of the Wonji fault belt (WFB). The location of MT stations at Aluto and Tulu Moye is indicated by the blue circles.

stage of differentiation in the lower crust, followed by a quick rise of magma toward the surface through existing conduits and subsequent further differentiation in a shallow magmatic mush zone (e.g. Rooney et al., 2007; Macdonald et al., 2008; Gleeson et al., 2017). Such two-level magmatic plumbing systems are well-documented in fossil rifts (e.g., the Ivrea-Verbano Zone, Northern Italy; Karakas et al. (2019)).

We focus on two major volcanic complexes in the CMER, namely Aluto and Tulu Moye. The two volcanoes are located 50 km apart at the WFB north and south of Lake Ziway (see Fig. 1 and supplemental Figure S1 for detailed maps of the area). At Aluto, caldera forming events occurred around 300 kaBP, and post-caldera activity resumed at $55 - 40$ ka (Hutchison et al., 2016b). The main volcanic edifice of Tulu Moye is located at the southern tip of a nested caldera system with large eruptions that have been dated at 1.77 Ma to 115 kaBP (Bigazzi et al., 1993). Both volcanic complexes are characterized by silicic post-caldera volcanism, comprising effusive rhyolitic lava-flows and explosive pyroclastic eruptions (Hutchison et al., 2016b; Fontijn et al., 2018). The youngest eruption at Aluto was of explosive type and took place around 400 years BP (Hutchison et al., 2016b). At Tulu Moye, the latest eruptions happened in the late nineteenth century in form of rhyolitic lava flows that outpoured through faults in clusters north of Tulu Moye volcano (Fontijn et al., 2018, and references therein).

Space-borne Synthetic Aperture Radar Interferometry (InSAR) measurements revealed significant ground deformations at several volcanoes in the CMER, including Aluto and Tulu Moye (Biggs et al., 2011). In an observation period from 2004 to 2011, Aluto experienced two cycles of rapid uplift, followed by longer periods of subsidence (Biggs et al., 2011; Hutchison et al., 2016a). Hitherto, no surface deformation was observed at Tulu Moye volcano itself. However, an area about 8 km west of the volcano was affected by continuous ground uplift in an observation period from 2008 to 2010 (Biggs et al., 2011; Samrock et al., 2018). The cause for the observed volcanic unrest is a topic of ongoing discussions.

For decades, geophysical surveys have been conducted in the Ethiopian rift to study rifting, magmatism and to image the internal structure and the dynamics of active volcanoes (Yirgu et al., 2006). Recent geophysical surveys conducted at Aluto and Tulu Moye include magnetotelluric (MT) (Samrock et al., 2015; Cherkose & Mizunaga, 2018; Hübert et al., 2018; Samrock et al., 2018, 2020) and seismic measurements (Wilks et al., 2017; Nowacki et al., 2018; Greenfield et al., 2019a). To date, electrical conductivity models derived from the MT data provide the only multi-scale, pan-crustal, 3-D subsurface images of both prospects.

2. MT data interpretation and models

MT is a passive geophysical sounding method that uses Earth's electromagnetic field variations to determine the electrical conductivity distribution in the Earth's subsurface. In volcanic systems, the electrical conductivity is dominated by factors such as the presence of melt, magmatic or meteoric brine and hydrothermal alteration minerals, such as smectite. These factors all appear as electrically conducting zones that can be well imaged by MT. At Aluto, MT surveys were conducted between 2009 and 2012 with the aims of geothermal exploration and characterizing volcanic unrest (Samrock et al., 2015; Cherkose & Mizunaga, 2018; Samrock et al., 2020). MT measurements at Tulu Moye were conducted in the context of a geothermal exploration program, starting in 2016 (Samrock et al., 2018). 3-D electrical conductivity subsurface models for Tulu Moye and Aluto (Fig. 1) were recovered by magnetotelluric phase tensor inversion and are presented in Samrock et al. (2018) and Samrock et al. (2020). As can be seen, the models for Aluto (Fig. 2A,C) and Tulu Moye (Fig. 2B,D) exhibit similar structural features, but differ in terms of size and magnitude of the anomalies. A common feature of both volcanic complexes is a prominent spatially extended conductor, C1, at shallow depths down to $\sim 2\,\mathrm{km}$ below the surface. Geothermal wells from Aluto confirm that C1 is related to the presence of smectite clay, which results from hydrothermal alteration of volcanic rocks on top of the convective hydrothermal reservoir (Cherkose & Mizunaga, 2018; Lévy et al., 2018). Below the clay cap, C1, a conductor, C2, appears at mid-crustal depths of $\sim 1-4$ km.b.s.l. at both Aluto and Tulu Moye. C2 is interpreted as a

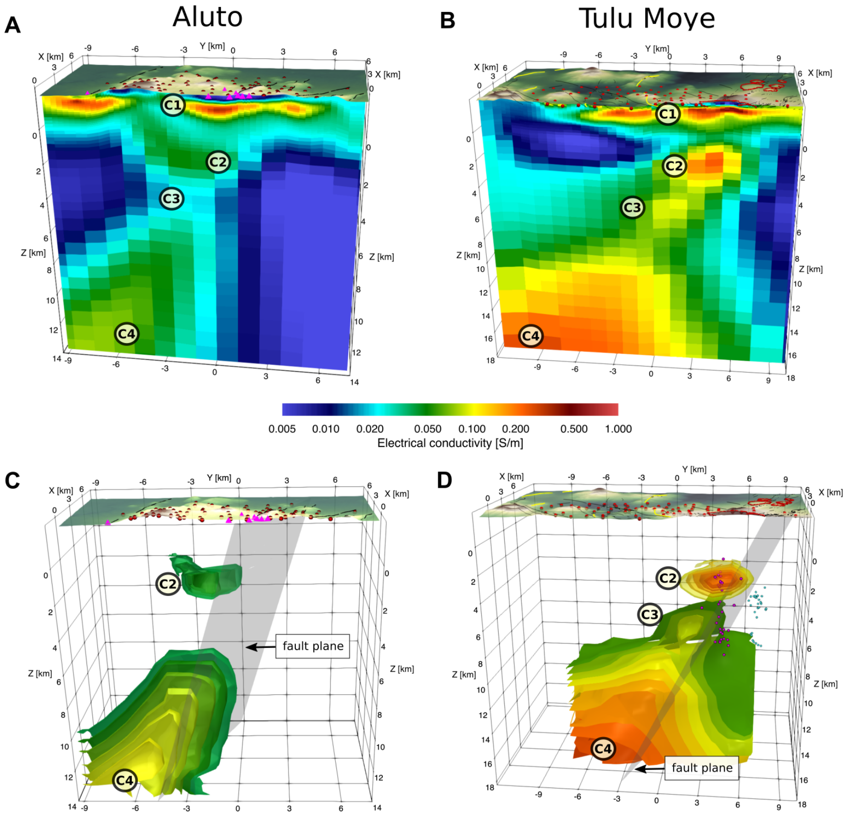

Figure 2: Electrical conductivity models of Aluto (A,C) and Tulu Moye (B,D) areas. The x-direction points to the North, y to the east. The z-coordinate is given with respect to sea level. Black lines indicate faults, red spheres locations of MT stations, red outlines indicate lava flows at Tulu Moye. Conductive zones are considered to represent (C4) the lower crustal zone of melt accumulation, (C3) the channel of focused melt ascent along faults into the shallow crustal melt zone (C2), and the clay cap (C1) on top of the convective hydrothermal system. The fault plane in (C,D) is a visual aid to indicate the dominant strike and dip of faults in the survey areas. Magenta triangles in (A) and (C) mark the locations of geothermal wells. Magenta and cyan spheres in (D) denote the location of low-frequency earthquakes subdivided into two main swarms (Greenfield et al., 2019a).

magmatic heat source for the overlying convecting hydrothermal reservoirs (located between C1 and C2). C2 is underlain by a deeper electrically conducting zone, C4, at depths below 8 km.b.s.l.. C4 is considered to be the lower crustal zone of melt accumulation and thus the parental magma reservoir, which is connected to the upper crustal melt reservoir, C2, via magmatic pathways, C3, that appear as an electrically conducting channel, following the dominant orientation of faults. Seismic studies in the CMER revealed that the source region of melt is within the upper mantle with an onset of decompression melting beneath the central rift axis, where crustal thicknesses are only $\sim 25-37$ km (Rychert et al., 2012).

The MT models from Aluto and Tulu-Moye are in striking agreement with the petrological findings that propose a transcrustal two-level magmatic system with magma ponding in the lower crust, C4, and quick rise of magma into the shallow crust into a zone of magma storage and fractional crystallization at $\sim 3.5-5$ km below the surface, C2 (Rooney et al., 2007, and references therein). However, a clear difference among the MT models is that the electrical conductivity values are systematically lower for the Aluto magmatic system compared to the Tulu Moye system (compare C2, C3 and C4 in Fig. 2A,C and B,D).

In order to better understand the nature of the observed differences, we developed a framework to link data sets from MT and petrological field observations with thermodynamic modelling of melt evolution and laboratory-based models for melt electrical conductivity. The capability of our new approach to characterize felsic magmatic systems is demonstrated for Aluto and Tulu Moye.

Note, earlier MT studies at Aluto by Samrock et al. (2015), Cherkose & Mizunaga (2018) and Hübert et al. (2018) did not image the conductors C2-C4 below the clay cap C1. One reason for the limited sensitivity of these surveys to the deeper conductors C2-C4 is the sparse spatial data coverage. The 3-D studies by Samrock et al. (2015) and Cherkose & Mizunaga (2018) are based on two different datasets that both comprise < 50 irregularly distributed sites at Aluto. The ~ 120 km long 2-D cross-rift MT profile by Hübert et al. (2018)

had only 2 MT stations over Aluto. Due to the absence of electrical conductors C2-C4 under Aluto in these earlier models, the existence of notable quantities of melt under Aluto was considered implausible. Conductors C2-C4 under Aluto were first imaged in the study by Samrock et al. (2020), which is based on a 3-D inversion of 165 MT stations with a regular distribution over the entire Aluto volcanic complex.

3. Linking geophysical and petrological observables through thermodynamic modelling

The standard methods to relate bulk electrical conductivity of a heterogeneous medium with volume fractions of its constituents rely on mixing models, such as Archie's law (e.g. Pommier, 2014). In studies of crustal magmatic systems, two-phase mixing laws are widely used to estimate melt volume fractions together with laboratory-based models for electrical melt conductivity and assumptions on the geometrical distribution of the melt (Hill et al., 2015; Hübert et al., 2018; Samrock et al., 2018; Laumonier et al., 2019). These interpretations typically test arbitrary combinations of pressure, P, temperature, T, and H_2O-content values to find plausible ranges that explain the observed geophysical variables. One significant limitation of this approach is that it does not require the chosen parameter range to be in agreement with composition-dependent melt equilibrium conditions.

3.1. Melt evolution modelling

Our primary motivation is to better constrain the parameters that determine the current state of felsic magma reservoirs, which are denoted as electrical conductors C2 (Fig. 2). The first step involves thermodynamic modelling using Rhyolite-MELTS (Gualda et al., 2012) to reproduce melt evolution and system phase fractions during the course of crystallization. In a cooling magmatic system the composition of the residual melt is predetermined by the composition of its parental melt and mineral phase stability during cooling and crystallization. The so-called "incompatible" elements (incompatible with the structure of the dominant mineral phases, such as SiO_2, H_2O), are enriched in the residual melt. As a consequence, the SiO_2-content of the residual melt increases with progressing crystallization from basaltic ($\sim 48-53$ wt% SiO_2) to andesitic ($\sim 52-63$ wt% SiO_2) to dacitic ($\sim 63-68$ wt% SiO_2) and to rhyolitic melt (> 68 wt% SiO_2). The thermodynamic modeling software Rhyolite-MELTS allows to calculate phase stability for various magmatic conditions and given starting compositions (Gualda et al., 2012). The modeling results are output in terms of the composition of the cooling residual melt, the growing solid and the magmatic volatile phase (MVP).

Gleeson et al. (2017) found through Rhyolite-MELTS that whole rock compositions of peralkaline rhyolites at Aluto can be reproduced by shallow ($P = 0.15$ GPa) isobaric fractionation of parental mafic melt with an initial H_2O-content of 0.5 wt%. The initial H_2O-content results in a pre-eruptive H_2O-content of 5 wt% as the melt reaches rhyolitic composition, in agreement with observed H_2O-contents in melt inclusions from the CMER (Iddon & Edmonds, 2020).

We followed the thermodynamic modeling strategy of Gleeson et al. (2017), but made two minor modifications; First, we use a newer version of Rhyolite-MELTS with an implemented H_2O-CO_2 fluid saturation model that accounts for the solubility of H_2O and CO_2 in natural silicic melts (see Ghiorso & Gualda, 2015). And, second, we used a more evolved starting composition than Gleeson et al. (2017) (Hutchison et al., 2016b, sample 15-01-07B). To account for the more evolved state of our starting sample we use a higher H_2O-content of 2 wt% and 0.3 wt% CO_2. These values are in agreement with inferred H_2O- and CO_2-contents from melt inclusions from the study region (Iddon & Edmonds, 2020). Our calculations yield a maximum of 72.5 wt% SiO_2 and an H_2O-content of 4.7 wt% at $T = 731.00\,^{\circ}\mathrm{C}$ within the remaining residual melt at the modelled pressure and temperature. The CO_2-content at the same stage is only 0.02 wt%, reflecting that the solubility of CO_2 in melt is very low after $> 75\%$ crystallization (see Fig. 3).

When investigating melt evolution using Rhyolite-MELTS, it is important

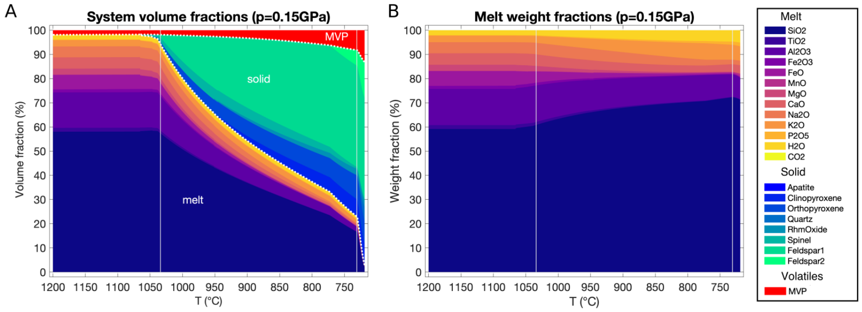

Figure 3: Melt, solid and magmatic volatiles phase (MVP) composition and fractions during the course of crystallization as predicted by Rhyolite-MELTS. (A) shows system volume fractions and (B) weight fractions within the melt phase only. At 1041 °C (vertical line) the melt composition corresponds to the andesitic melt model by Guo et al. (2017). We use this temperature as the starting point for the electrical conductivity calculations. At 731 °C (vertical line) the system reaches high crystallinities ($> 75\,\%$) and the amount of the MVP exceeds 5 vol%.

to bear in mind that this thermodynamic modelling tool is calibrated from experimental results on the composition of melt and solids over a wide range of temperatures and pressures. As a consequence, the results can be partly inaccurate due to lack of experimental data on alkalic magmas such as those of Aluto, especially when reaching high crystallinities.

We note that our calculation seems to underestimate the Na_2O-content in the melt due to over-stabilization of feldspar in the simulation. However, an in-depth investigation on the details of phase stability and melt composition is beyond the scope of this study. Bearing these limitations in mind, we believe that the fractions of the individual phases during the course of crystallization as well as the SiO_2- and H_2O-contents within the residual melt are modelled accurately enough, to provide robust results for our study.

The key advantage of the newest version of Rhyolite-MELTS is the refined calibration of the behaviour of H_2O and CO_2 in the magma (including their coupled solubilities). Hence, the model simulations allow us to track the amount of exsolved H_2O and CO_2 (forming a Magmatic Volatile Phase or MVP) as the magma crystallizes, the so-called second boiling effect (e.g. Candela, 1997). As the system reaches high crystallinities ($\geq 70 - 80\,\text{vol}\%$ crystals, $T < 730\,^{\circ}\text{C}$), the amount of the MVP is predicted to be in excess of 5 vol% (Fig. 3A, see also Parmigiani et al. (2017) for similar results with slightly different conditions), making it an important component in determining the electrical conductivity at high crystal fractions (”mush” state of the magma reservoir).

3.2. Electrical conductivities of the individual phases

In the second step we derive the electrical conductivities, σ_{melt}, σ_{solid} and σ_{MVP} of all three phases within the modelled magmatic system.

Laboratory measurements of the electrical conductivity of natural silicic melt are critical to interpret MT subsurface models and to understand subsurface properties of the Earth. The principles of laboratory techniques to study electrical properties of melt at conditions prevailing in the Earth’s interior are e.g. presented in reviews by Pommier (2014) and Ni et al. (2015). Here we summarize the key mechanisms that control melt electrical conductivity. The electrical conductivity of silicic melt is controlled by the mobility of its charge carriers. Experiments show that the main charge carriers in silicic melt are alkali metals, particularly sodium (Na). Depending on the sodium concentration, it can contribute to more than 80 % of the total electrical conductivity of dry silicic melt (Pommier, 2014, and references therein). The mobility of sodium shows an anti-compositional trend and increases with increasing viscosity, i.e. increasing SiO_2-content, of the melt. As a consequence silicic melt tends to become more electrically conductive with progressing fractional crystallization. A general relationship between sodium content and electrical conductivity of melt, as suggested in the Nernst-Einstein-equation, is difficult to set up. The diffusivity of Na in melt is also controlled by the remaining melt components, particularly potassium (Ka) has a non-trivial concentration-dependent effect on the mobility of sodium in melt (Fig. 18, Ni et al., 2015). Dissolved water has a strong impact on melt electrical conductivity. Adding 1 wt% of dissolved H_2O leads to a 1.3 to 2.5-fold increase of the melt’s electrical conductivity (see Fig. 4 below). The solubility of CO_2 in silicic melt at low pressures is small and a low concentration of CO_2 has no noticeable effect on electrical conductivity (Lowenstern, 2001; Ni et al., 2015).

Experiment-calibrated models of the electrical conductivity of natural silicic melt, σ_{melt}, typically provide a mathematical expression that describes the electrical conductivity for a specific melt composition as a function of pressure, P, temperature, T, and H_2O-content: $\sigma_{melt}(P, T, H_2O)$. For this study we expand this model by introducing a fourth dependency of σ_{melt} on SiO_2-content through a second-order polynomial interpolation between existing melt electrical conductivity models for andesite (Guo et al. (2017); 60.8 wt% SiO_2), dacite (Laumonier et al. (2019); 65.8 wt% SiO_2) and rhyolite (Guo et al. (2016); 75.7 wt% SiO_2). These melt models are the latest available in literature and they are valid at temperatures, pressures and H_2O-contents as predicted by our melt evolution model (Fig. 3B). Detailed information about the individual melt models is provided in the supplementary materials.

We chose the approach of interpolating between existing models as the only practical solution to overcome the lack of experiment-constraint composition-depended electrical conductivity models for silicic melt. The result is a generalized model for the electrical conductivity of the liquid melt phase $\sigma_{melt}(P, T, SiO_2, H_2O)$ (see Figs. 4 and S2). The positive trend of σ_{melt} with increasing SiO_2 and H_2O-content confirms the dominating conduction mechanisms, which are increasing mobility of the dominant charge carriers with SiO_2-content and the positive effect of temperature and dissolved H_2O on electrical conductivity (Ni et al., 2015).

Using the derived functional dependency we calculated the electrical melt conductivity $\sigma_{melt}(P, T, SiO_2, H_2O)$, where P, T, SiO_2- and H_2O-content are given by RhyoliteMELTS modelling (Fig. 2B). The resulting electrical conductivity of our modelled melt phase is shown in Fig. 5 (see also Fig. S2). σ_{melt} varies between 0.6 S/m at high temperatures, increasing to a maximum of 1.2 S/m at around 850 °C, to decrease again to about 1 S/m at lower temperatures of 730 °C. Note that variations of σ_{melt} appear to be moderate at temperatures below 950 °C, where it stays close to 1 S/m (Fig. 4). This results from

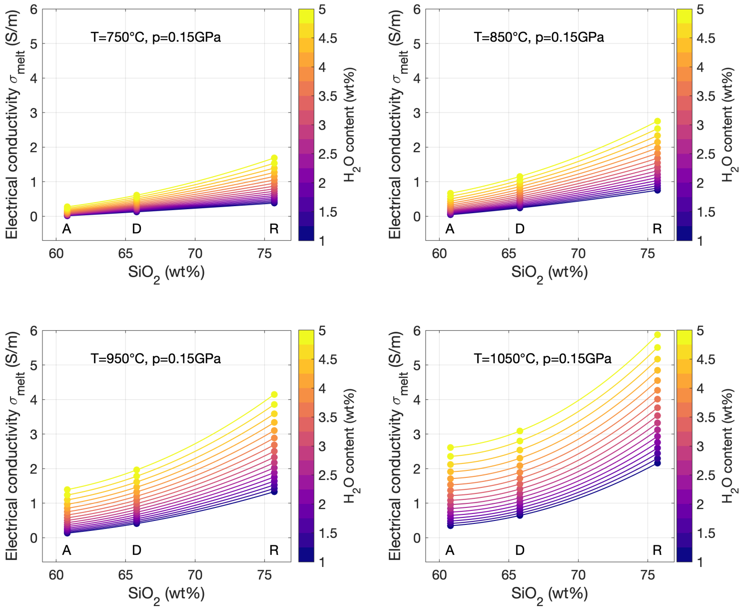

Figure 4: Electrical conductivity σ_{melt} for andesite (A: 60.8 wt% SiO_2, Guo et al. (2017)), dacite (D: 65.8 wt% SiO_2, Laumonier et al. (2019)) and rhyolite melt (R: 75.7 wt% SiO_2, Guo et al. (2016)). σ_{melt} is shown at four different temperatures, a fixed pressure of 0.15 GPa and H_2O-contents between 1 and 5 wt%. The families of curves show second order polynomial fits we used to interpolate between the three models to obtain the dependence of σ_{melt} on SiO_2-content.

a counterbalancing effect, where decreasing σ_{melt}, with lower temperatures is compensated by the increasing H_2O-content within the melt and the increased mobility of the dominant charge carriers.

For the crystallized solid in the three-phase magmatic system, we assigned an electrical conductivity of $\sigma_{solid} = 0.005\,\mathrm{S/m}$, which is representative for intact crust, surrounding the magmatic systems (cf. Fig. 2). The conductivity of $\sigma_{solid} = 0.005\,\mathrm{S/m}$ also corresponds to experiment-constraint electrical conductivities of Gabbro at crustal pressures and temperatures of $450 - 550\,^\circ\mathrm{C}$ (Dai et al., 2015). Electrically resistive bodies in this part of the CMER are commonly interpreted as crystallized gabbroic crustal magmatic intrusions (Hübert et al., 2018, and references therein).

The magmatic volatiles represent the third phase. Given the modelled temperature and pressure conditions, it is in a supercritical state (Driesner & Heinrich, 2007). When reaching supercritical conditions, the electrical conductivity of geothermal fluids is known to decrease significantly (Kummerow et al., 2018). Here we assign the magmatic volatile phase the experimentally determined electrical conductivity, $\sigma_{MVP} = 0.01\,\mathrm{S/m}$, of a slightly saline NaCl-bearing aqueous solution at a temperature of $T = 710\,^{\circ}\mathrm{C}$ and a pressure of $P = 0.15\,\mathrm{GPa}$ (Quist & Marshall (1969); see supplementary Figure S3).

Note, a limitation of Rhyolite MELTS is that only H_2O and CO_2 are considered as components of the free magmatic volatile phase, MVP. The program is not calibrated to model dissolution of minerals into the volatile phase. Since very few data are available for the electrical conductivity of supercritical brines we used observed values from experiments by Quist & Marshall (1969), which were conducted in our modelled temperature and pressure range. The study by Quist & Marshall (1969) is in overall good agreement with more recent results by Kummerow et al. (2018), who conducted similar experiments to study the electrical conductivity of supercritial geothermal fluids at lower temperatures

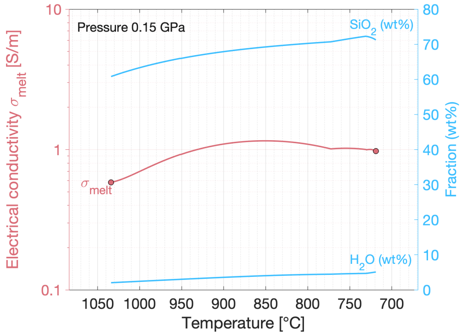

Figure 5: Electrical conductivity $\sigma_{melt}(P, T, \mathrm{SiO_2}, \mathrm{H_2O})$ of the melt phase (Fig. 2B) with cooling temperature during the course of fractional crystallization and at a fixed pressure of 0.15 GPa. The right y-axis indicates the evolution of the H_2O- and SiO_2-content within the residual melt. $\sigma_{melt}(P, T, \mathrm{SiO_2}, \mathrm{H_20})$ was derived as described in the main text.

and pressures.

3.3. Bulk electrical conductivity of a three-phase magmatic system

To derive the bulk electrical conductivity, σ_{bulk}, of the modelled magmatic system consisting of crystalline solid, liquid melt and magmatic volatiles, we employ a generalized Archie's law for three phases (Glover, 2010). The law is advantageous due to its generalized formulation for n phases and concepts for connectedness and conservation of connectedness. The generalized Archie's law is given by:

$$\sigma_{bulk} = \sum_{i=1}^{n} \sigma_i \phi_i^{m_i}, \tag{1}$$

subject to

$$\sum_{i=1}^{n} G_i = \sum_{i=1}^{n} \phi_i^{m_i} = 1. \tag{2}$$

Eq. 1 describes the bulk electrical conductivity of a system with n phases, with conductivities σ_i, volume fractions ϕ_i and cementation exponents m_i. The conservation of connectedness is ensured by Eq. 2, which states that the sum of the connectednesses, G_i, is equal to unity. Note, here we follow the nomenclature of Glover (2010), who introduced the phrase *connectedness* to distinguish from *connectivity*, which is a different entity.

The electrical conductivities σ_i in Eq. 1 for the three phases are given as previously described. The related phase fractions, ϕ_i, are given by the MELTS modelling (Fig. 2A). Note, for calculating the evolution of the bulk electrical conductivity σ_{bulk} of the crystallizing magmatic system we start with an initial overall melt-to-solid-ratio of $60 : 40\,\mathrm{vol\%}$. The cementation exponents, m_i, represent a geometrical description of the interconnectivity of the phases. In general, m_i increases as the degree of connectedness of the ith phase decreases (Glover, 2010). We treat the cementation exponents, m_i, in our three-phase system as variables that change according to structural changes within the melt-crystal mixture over the course of crystallization. Analytical solutions for the cementation exponent exist for a fully connected phase, $m = 1$, and for liquids embedded in an assemblage of perfect spheres, $m = 1.5$ (Glover, 2010, and references therein). Experimentally determined cementation exponents exist for crystalline mush, $m = 1.73$ (Jahrling & Tait, 1996), and for saline liquids in freezing permafrost soil, where m increases from 1.81 to 2.1 as water freezes (crystallizes) (Wu et al., 2017).

We assume that the melt phase in the magmatic system is fully connected ($m_{melt} = 1$) until the total melt fraction falls below $\phi_{melt} = 0.4$, i.e. 40 vol%, then m_{melt} follows a linear increase with decreasing melt fraction until it reaches $m_{melt} = 2.1$ in a fully crystallized system:

$$m_{melt} = \begin{cases} 1 & \phi_1 > 0.4 \\ -2.75\phi_1 + 2.1 & \phi_1 < 0.4 \end{cases} \tag{3}$$

For the free magmatic volatile phase we assign a constant formation factor of $m_{MVP} = 1.5$, representing a moderately interconnected interstitial phase (Glover, 2010).

The cementation exponent for the solid phase is calculated such that the conservation of connectedness (eq. 2) is satisfied. The resulting values for phase fractions ϕ_i, cementation exponents m_i, and connectednesses G_i we used to calculate σ_{bulk} are shown in Fig. 6. The figure also shows the parameter interval for the tolerance range $\delta\sigma_{bulk}$ (Fig. 7), which provides insight into the sensitivity of σ_{bulk} to variations of the initial melt fraction, and cementation exponents m_i. The tolerance range $\delta\sigma_{bulk}$ includes a range of initial melt fractions, ϕ_{melt}, from

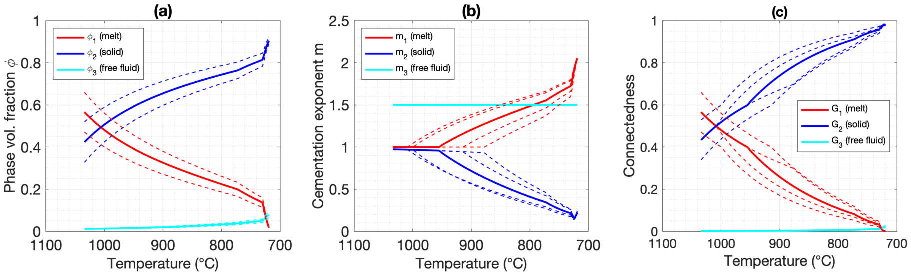

Figure 6: Parameters with cooling temperatures to calculate σ_{bulk} using eqs. 1 - 3: (a) phase fraction Φ_i, (b) formation factor m_i and (c) connectedness G_i. The dashed lines indicate the parameter interval we used to calculate the tolerance range $\delta\sigma_{bulk}$ (see Fig. 7).

0.5 to 0.7. The variations of m_{melt} are calculated as in eq. 3 but explore a range of perfect connectedness $m_{melt} = 1$ until a melt fraction of 0.3 and 0.5, respectively.

The resulting electrical conductivity σ_{bulk} is shown in Fig. 7 together with the phase fractions within the modelled magmatic system. At high melt fractions of $\phi_{melt} > 40\,\mathrm{vol\%}$ σ_{bulk} of the magmatic system varies between 0.3-0.4 S/m. With progressing crystallization σ_{bulk} decreases by one order of magnitude from $\sim 0.4\,\mathrm{S/m}$ at 950 °C and 40 vol% melt fraction to $\sim 0.04\,\mathrm{S/m}$ at 730 °C and $\sim 13\,\mathrm{vol\%}$ melt fraction. At temperatures below 730 °C σ_{bulk} decreases rapidly, which is related to the increased rate of crystallisation and, as a consequence thereof, increased volatile degassing. In this highly crystalline state of the magmatic system the high MVP content of $\sim 5-8\,\mathrm{vol\%}$ has a small but non-neglible influence and lowers electrical conductivity of the magmatic system

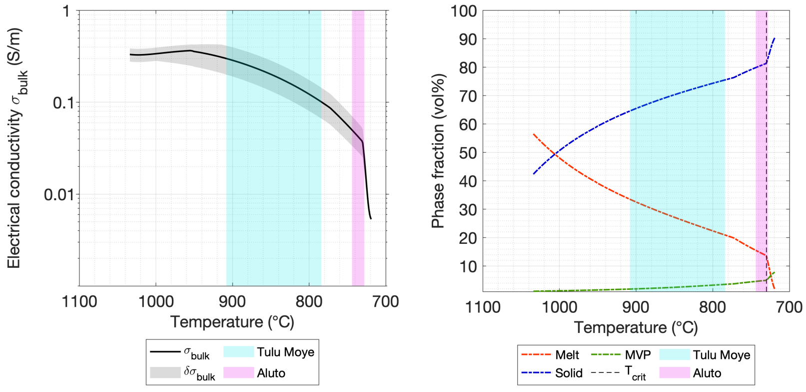

Figure 7: Evolution of the bulk electrical conductivity σ_{bulk} of the modelled silicic magmatic system during the course of fractional crystallization assuming an initial overall melt content of 60 vol%. The envelope indicates the tolerance range $\delta\sigma_{bulk}$ for different initial melt contents ($50 - 70\,\mathrm{vol\%}$) and variations of the connectednesses, G_i, of the individual phases (see supplementary materials for details). The right-hand y-axis shows the phase fractions. The respective states of the magmatic systems C2 under Tulu Moye and Aluto are indicated by magenta triangles and cyan stars.

from 0.04 S/m down to less than 0.01 S/m in the fully crystallized system. The effect of the magmatic volatiles on σ_{bulk} is shown in Fig. 8. As can be seen, the phase space trajectory of the magmatic system is attracted to lower electrical conductivities with increasing MVP fraction when compared to a two-phase system consisting of melt and solid only. Considering the magmatic reservoir as a three-phase system highlights the importance of including magmatic volatiles as a third phase in order to understand the sometimes low electrical conductivities within magmatic systems.

Our results show that the differences in electrical conductivity ranges within the magmatic systems under Aluto and Tulu Moye (C2 in Fig. 2), likely reflect different stages of melt evolution. Compared to Aluto, the magmatic system under Tulu Moye with conductivies of $0.1 - 0.3$ S/m in C2 is likely hotter (780 to 910 °C in its hottest innermost part) and contains about $20 - 33$ vol% melt (see Fig. 7). In contrast, Aluto's upper crustal reservoir with conductivities of $0.03 - 0.05$ S/m in C2 is colder and more crystalline, with only $\sim 10 - 15$ vol% melt, but higher MVP content (> 5 vol% within C2). The high MVP content

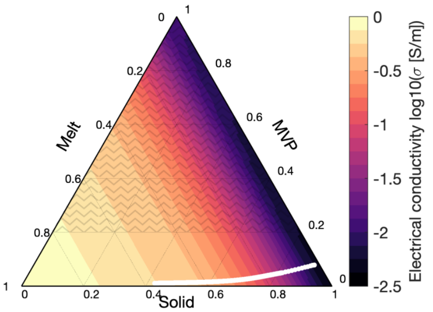

Figure 8: Ternary diagram showing the bulk electrical conductivity of a three phase system consisting of different fractions of solid, melt and a magmatic volatile phase (MVP). The electrical conductivity was calculated as described in the main text, but assuming $\sigma_{melt} = const. = 1$ S/m. The white line indicates the phase space trajectory of our modelled magmatic system during the course of fractional crystallization. Note, our assumptions about the cementation exponents (Fig. 6) are not considered to be valid for high MVP fractions of > 0.2 (hashed area).

induces increased volatile degassing in Aluto (see Fig. 7).

4. Discussion

Electrical conductivity derived from MT images is often used to interpret magmatic reservoirs. This study proposed to use a more elaborated three-phase system to model bulk electrical properties. Compared to previous studies, a notable difference is the inclusion of a magmatic volatile phase. Additionally, complex magmatic systems were modelled by invoking a thermodynamic phase equilibria approach that can be constrained by insitu petrological samples. As applied to two volcanoes in the Ethiopian Rift this approach leads to estimates on key parameters of the magmatic systems, such as melt content, temperature and volatile abundance. Our results from Aluto and Tulu Moye are further supported by seismicity records: the seismicity at Aluto is concentrated in the upper 2 km below surface. A large overall b-value of 1.4 ± 0.14 indicates an elevated number of small magnitude events, which Wilks et al. (2017) interpreted to be predominantly fluid-induced, supporting our findings that Aluto is in a state of enhanced volatile degassing. Nowacki et al. (2018) related a strong shear wave anisotropy under Aluto to WFB-aligned cracks, that are held open by over-pressurized fluids. Most shear wave splitting occurs at depths shallower than 3'000 m.b.s.l., co-located with the degassing magmatic system, C2, and the hydrothermal reservoir (between C1 and C2). In a more recent study, Wilks et al. (2020) presented the first seismic tomography model of Aluto volcano. Their seismic model shows high v_p/v_s regions at depths consistent with our conductors C2 and C3, which can be interpreted as zones with partial melt, thus consistent with our MT model.

Seismicity at Tulu Moye differs from Aluto to the effect that most seismicity occurs at 0.5-1 km b.s.l depths, with only a small fraction of shallow earthquakes (Greenfield et al., 2019b). Comparable to Aluto, an overall b-value of 1.32 ± 0.14 suggests that fluid-flow-induced failure of existing, weak fractures and faults is the predominant seismogenic mechanism. A series of low-frequency earthquakes, that occur in two clusters (see Fig. 2D) beneath the Tulu Moye volcano and the youngest lava flows, was interpreted to be caused by fluid pulses, originating from a shallow magma body, entering a highly fractured region (Greenfield et al., 2019a). A large fraction of low-frequency events of the western swarm occurs within the electrical conductor C2. According to our interpretation, C2 under Tulu Moye reaches a maximum bulk content of ~ 33 vol% melt. However, the inferred constraint does not rule out that C2 may contain isolated melt-rich lenses that are preferably oriented along the Wonji faults. Low-frequency seismicity can be attributed to brittle failure of such crystal-rich silicic mush, either by slow-rupture of the magma itself or by enforcing the formation of pathways for gas release and conduit excitation (Tuffen et al., 2008).

The origin of non-eruptive ground deformations at Aluto and Tulu Moye has been the subject of debate since its discovery by Biggs et al. (2011). Initial hypotheses related ground deformation to shallow magma injection. However, MT and seismicity studies found no evidence for ongoing melt movement under Aluto (Samrock et al., 2015; Wilks et al., 2017). As a consequence, alternative explanations were brought forward that argued in favour of perturbations of the hydrothermal system being triggered by exsolved magmatic volatiles, which can explain both periods of ground uplift and periods of subsidence during non-eruptive volcanic unrest (Samrock et al., 2015; Hutchison et al., 2016a; Wilks et al., 2017). Our results indicate that the imaged body C2 under Aluto is a highly crystalline, stagnant, but degassing magmatic body. There are no indications for *magma on the move* as a source of the observed ground deformations. Instead, two dominating mechanisms, or a combination of both, likely trigger reoccurring periods of uplift and subsidence at Aluto: (i) elastic expansion of the highly crystalline magmatic body itself, related to expansion of an exsolved MVP (Chouet & Matoza, 2013) and, (ii), inflation of the hydrothermal system due to thermoelastic expansion and pressurization by the injection of magmatic volatiles (Chiodini et al., 2016).

For the Tulu Moye area deformation time-series are limited to a time span from March 2008 to October 2010, where continuous uplift with an averaged speed of 2 cm/yr was observed in an area about 8 km west of the imaged intrusion C2 (Biggs et al., 2011; Samrock et al., 2018). However, our current MT model does not exhibit the existence of an inflating magmatic source directly under the center of deformation west of Tulu Moye volcano (Samrock et al., 2018). This indicates that understanding the processes behind volcanic unrest and their associated surface signals requires an interdisciplinary approach and physically elaborated models (Gottsmann et al., 2020). A detailed investigation of volcanic unrest near Tulu Moye is beyond the scope of this study, however, Hickey et al. (2016) showed that deformation source locations can change substantially if topography and subsurface heterogeneities are accounted for in deformation analyses.

5. Conclusion

Our study provides a self-consistent interpretation of the magmatic systems of two volcanoes in the Ethiopian Rift and demonstrates how different data sets and observations can be brought together to better image and constrain the current status of active magmatic systems. The study has implications for understanding magmatic processes beneath volcanoes at both micro- and macro-scales, which plays a key role in assessing volcanic hazards. Our results suggest that Tulu Moye, which erupted very recently, has a hotter, less crystalline upper crustal reservoir than Aluto. Hence, Tulu Moye may be closer to another eruption than Aluto. This latter would require a significant recharge from the lower crust to reactivate the highly crystalline shallow reservoir and allow magma to reach the surface.

Furthermore, the results are important for gaining insight into the formation of geothermal resources and mineral deposits. Geothermal energy utilization using volcanic resources is currently experiencing a strong upsurge in countries along the East African Rift. With temperatures that exceed 730 °C, the shallow magmatic intrusions under Aluto and Tulu Moye represent lasting heat sources to power ongoing and future geothermal energy production in Ethiopia.

Acknowledgements

This work was supported by a grant from the Swiss National Supercomputing Centre (CSCS) under project ID907. M.O.S. and F.S. thank the Werner Siemens Foundation for their endowment of the Geothermal Energy and Geofluids group at ETH Zurich. A.G. was partly supported by the ESA Swarm DISC program. The work by O.B. was partially supported by grant SNF #200021_178928. We acknowledge the use of Generic Mapping Tools (GMT) and thank NASA for providing SRTM digital elevation models. We thank the reviewers Kate Selway and Martyn Unsworth for thoughtful and constructive comments, which helped to improve the manuscript.

Appendix A. Supplementary material

The supplementary material for this paper is provided as a separate file that includes information on the MT surveys and detailed maps from Aluto and Tulu Moye (Text S1, Figure S1), technical information on the melt electrical conductivity models (Text S2, Table S1, Figure S2) and on the electrical conductivity of fluids up to supercritical conditions (Text S3, Figure S3). Details about the estimation of the bulk electrical conductivity using a three-phase Archie's law are provided in Text S4 and Figure S4.

An animation showing the evolution of σ_{melt} with progressing fractional crystallization is shown in Movie S1, which is uploaded separately. In addition we provide the output data file of our RhyoliteMELTS modelling. This file contains the continuous record of the evolution of the magmatic system in terms of state and composition at every stage in the model calculation.

Data availability

In this paper we present a method to link existing geophysical and petrological observations and models through thermodynamic modelling of melt evolution. The geophysical models, petrological data, thermodynamic modelling tools and techniques used in the quantitative interpretation are presented in this manuscript or are available from the cited publications.

References

Bachmann, O., & Huber, C. (2016). Silicic magma reservoirs in the Earth's crust. *Am. Mineral.*, *101*, 2377–2404. doi:10.2138/am-2016-5675.

Bigazzi, G., Bonadonna, F., Di Paola, G., & Giuliani, O. (1993). K-ar and fission track ages of the last volcano tectonic phase in the Ethiopian Rift Valley (Tullu Moye Area). *Geology and mineral resources of Somalia and surrounding regions*, (pp. 311–322).

Biggs, J., Bastow, I., Keir, D., & Lewi, E. (2011). Pulses of deformation reveal frequently recurring shallow magmatic activity beneath the Main Ethiopian Rift. *Geochem., Geophys., Geosyst.*, *12*. doi:10.1029/2011gc003662.

Birhanu, Y., Bendick, R., Fisseha, S., Lewi, E., Floyd, M., King, R., & Reilinger, R. (2016). GPS constraints on broad scale extension in the Ethiopian Highlands and Main Ethiopian Rift. *Geophysical Research Letters*, *43*, 6844–6851. doi:10.1002/2016gl069890.

Candela, P. A. (1997). A review of shallow, ore-related granites: textures, volatiles, and ore metals. *J. Petrol.*, *38*, 1619–1633. doi:10.1093/petroj/38.12.1619.

Cashman, K. V., Sparks, R. S. J., & Blundy, J. D. (2017). Vertically extensive and unstable magmatic systems: a unified view of igneous processes. *Science*, *355*, eaag3055. doi:10.1126/science.aag3055.

Cherkose, B. A., & Mizunaga, H. (2018). Resistivity imaging of Aluto-Langano geothermal field using 3-D magnetotelluric inversion. *J. Afr. Earth. Sci.*, *139*, 307–318. doi:10.1016/j.jafrearsci.2017.12.017.

Chiodini, G., Paonita, A., Aiuppa, A., Costa, A., Caliro, S., De Martino, P., Acocella, V., & Vandemeulebrouck, J. (2016). Magmas near the critical degassing pressure drive volcanic unrest towards a critical state. *Nat. Commun.*, *7*, 13712. doi:`10.1038/ncomms13712`.

Chouet, B. A., & Matoza, R. S. (2013). A multi-decadal view of seismic methods for detecting precursors of magma movement and eruption. *J. Volcanol. Geotherm. Res.*, *252*, 108–175. doi:`10.1016/j.jvolgeores.2012.11.013`.

Comeau, M. J., Unsworth, M. J., Ticona, F., & Sunagua, M. (2015). Magnetotelluric images of magma distribution beneath Volcán Uturuncu, Bolivia: Implications for magma dynamics. *Geology*, *43*, 243–246. doi:`10.1130/g36258.1`.

Corti, G. (2009). Continental rift evolution: from rift initiation to incipient break-up in the Main Ethiopian Rift, East Africa. *Earth-Sci. Rev.*, *96*, 1–53. doi:`10.1016/j.earscirev.2009.06.005`.

Dai, L., Hu, H., Li, H., Hui, K., Jiang, J., Li, J., & Sun, W. (2015). Electrical conductivity of gabbro: the effects of temperature, pressure and oxygen fugacity. *European Journal of Mineralogy*, *27*, 215–224. doi:`10.1127/ejm/2015/0027-2429`.

Driesner, T., & Heinrich, C. A. (2007). The system H_2O-NaCl. Part I: Correlation formulae for phase relations in temperature–pressure–composition space from 0 to $1000°C$, 0 to 5000 bar, and 0 to 1 X_{NaCl}. *Geochim. Cosmochim. Acta*, *71*, 4880–4901. doi:`10.1016/j.gca.2006.01.033`.

Fontijn, K., McNamara, K., Tadesse, A. Z., Pyle, D. M., Dessalegn, F., Hutchison, W., Mather, T. A., & Yirgu, G. (2018). Contrasting styles of post-caldera volcanism along the Main Ethiopian Rift: Implications for contemporary volcanic hazards. *J. Volcanol. Geotherm. Res.*, *356*, 90–113. doi:`10.1016/j.jvolgeores.2018.02.001`.

Ghiorso, M. S., & Gualda, G. A. (2015). An $H_2O - CO_2$ mixed fluid saturation model compatible with rhyolite-MELTS. *Contrib. Mineral. Petrol.*, *169*, 53. doi:10.1007/s00410-015-1141-8.

Gleeson, M. L., Stock, M. J., Pyle, D. M., Mather, T. A., Hutchison, W., Yirgu, G., & Wade, J. (2017). Constraining magma storage conditions at a restless volcano in the Main Ethiopian Rift using phase equilibria models. *J. Volcanol. Geotherm. Res.*, *337*, 44–61. doi:10.1016/j.jvolgeores.2017.02.026.

Glover, P. W. (2010). A generalized Archie's law for n phases. *Geophysics*, *75*, E247–E265. doi:10.1190/1.3509781.

Glover, P. W., Hole, M. J., & Pous, J. (2000). A modified Archie's law for two conducting phases. *Earth Planet. Sci. Lett.*, *180*, 369–383. doi:10.1016/s0012-821x(00)00168-0.

Gottsmann, J., Biggs, J., Lloyd, R., Biranhu, Y., & Lewi, E. (2020). Ductility and compressibility accommodate high magma flux beneath a silicic continental rift caldera: Insights from Corbetti caldera (Ethiopia). *Geochem. Geophys. Geosyst.*, *n/a*, e2020GC008952. doi:10.1029/2020gc008952.

Greenfield, T., Keir, D., Kendall, J.-M., & Ayele, A. (2019a). Low-frequency earthquakes beneath Tullu Moye volcano, Ethiopia, reveal fluid pulses from shallow magma chamber. *Earth Planet. Sci. Lett.*, *526*, 115782. doi:10.1016/j.epsl.2019.115782.

Greenfield, T., Keir, D., Kendall, J.-M., & Ayele, A. (2019b). Seismicity of the Bora-Tullu Moye Volcanic Field, 2016–2017. *Geochem. Geophys. Geosyst.*, *20*, 548–570. doi:10.1029/2018GC007648.

Gualda, G. A., Ghiorso, M. S., Lemons, R. V., & Carley, T. L. (2012). Rhyolite-MELTS: a modified calibration of MELTS optimized for silica-rich, fluid-bearing magmatic systems. *J. Petrol.*, *53*, 875–890. doi:10.1093/petrology/egr080.

Guo, X., Li, B., Ni, H., & Mao, Z. (2017). Electrical conductivity of hydrous andesitic melts pertinent to subduction zones. *J. Geophys. Res. Solid Earth*, *122*, 1777–1788. doi:`10.1002/2016JB013524`.

Guo, X., Zhang, L., Behrens, H., & Ni, H. (2016). Probing the status of felsic magma reservoirs: Constraints from the P–T–H2O dependences of electrical conductivity of rhyolitic melt. *Earth Planet. Sci. Lett.*, *433*, 54–62. doi:`10.1016/j.epsl.2015.10.036`.

Hickey, J., Gottsmann, J., Nakamichi, H., & Iguchi, M. (2016). Thermomechanical controls on magma supply and volcanic deformation: application to aira caldera, japan. *Sci. Rep.*, *6*, 32691. doi:`10.1038/srep32691`.

Hill, G. J., Bibby, H. M., Ogawa, Y., Wallin, E. L., Bennie, S. L., Caldwell, T. G., Keys, H., Bertrand, E. A., & Heise, W. (2015). Structure of the Tongariro Volcanic system: insights from magnetotelluric imaging. *Earth Planet. Sci. Lett.*, *432*, 115–125. doi:`10.1016/j.epsl.2015.10.003`.

Hübert, J., Whaler, K., & Fisseha, S. (2018). The electrical structure of the central main Ethiopian Rift as imaged by magnetotellurics: implications for magma storage and pathways. *J. Geophys. Res. Solid Earth*, *123*, 6019–6032. doi:`10.1029/2017jb015160`.

Hutchison, W., Biggs, J., Mather, T. A., Pyle, D. M., Lewi, E., Yirgu, G., Caliro, S., Chiodini, G., Clor, L. E., & Fischer, T. P. (2016a). Causes of unrest at silicic calderas in the East African Rift: New constraints from InSAR and soil-gas chemistry at Aluto volcano, Ethiopia. *Geochem. Geophys. Geosyst.*, *17*, 3008–3030. doi:`10.1002/2016gc006395`.

Hutchison, W., Pyle, D. M., Mather, T. A., Yirgu, G., Biggs, J., Cohen, B. E., Barfod, D. N., & Lewi, E. (2016b). The eruptive history and magmatic evolution of Aluto volcano: new insights into silicic peralkaline volcanism in the Ethiopian Rift. *J. Volcanol. Geotherm. Res.*, *328*, 9–33. doi:`10.1016/j.jvolgeores.2016.09.010`.

Iddon, F., & Edmonds, M. (2020). Volatile-rich magmas distributed through the upper crust in the Main Ethiopian Rift. *Geochem. Geophys. Geosyst.*, *21*, e2019GC008904. doi:`10.1029/2019gc008904`.

Jahrling, K., & Tait, S. (1996). Measurements of the evolution of porosity in a mushy layer. *J. Cryst. Growth*, *167*, 285–291. doi:`10.1016/0022-0248(96)00241-2`.

Karakas, O., Wotzlaw, J.-F., Guillong, M., Ulmer, P., Brack, P., Economos, R., Bergantz, G. W., Sinigoi, S., & Bachmann, O. (2019). The pace of crustal-scale magma accretion and differentiation beneath silicic caldera volcanoes. *Geology*, *47*, 719–723. doi:`10.1130/g46020.1`.

Kummerow, J., Raab, S., Schuessler, J. A., & Meyer, R. (2018). Non-reactive and reactive experiments to determine the electrical conductivities of aqueous geothermal solutions up to supercritical conditions. *J. Volcanol. Geotherm. Res.*, . doi:`10.1016/j.jvolgeores.2018.05.014`.

Laumonier, M., Karakas, O., Bachmann, O., Gaillard, F., Lukács, R., Seghedi, I., Menand, T., & Harangi, S. (2019). Evidence for a persistent magma reservoir with large melt content beneath an apparently extinct volcano. *Earth Planet. Sci. Lett.*, *521*, 79–90. doi:`10.1016/j.epsl.2019.06.004`.

Lévy, L., Gibert, B., Sigmundsson, F., Flóvenz, Ó. G., Hersir, G., Briole, P., & Pezard, P. (2018). The role of smectites in the electrical conductivity of active hydrothermal systems: electrical properties of core samples from Krafla volcano, Iceland. *Geophys. J. Int.*, *215*, 1558–1582. doi:`10.1093/gji/ggy342`.

Lowenstern, J. B. (2001). Carbon dioxide in magmas and implications for hydrothermal systems. *Mineralium Deposita*, *36*, 490–502. doi:`10.1007/s001260100185`.

Macdonald, R., Belkin, H., Fitton, J., Rogers, N., Nejbert, K., Tindle, A., & Marshall, A. (2008). The roles of fractional crystallization, magma mixing, crystal mush remobilization and volatile–melt interactions in the genesis of a young basalt–peralkaline rhyolite suite, the Greater Olkaria Volcanic Complex, Kenya Rift Valley. *J. Petrol.*, *49*, 1515–1547. doi:10.1093/petrology/egn036.

Ni, H., Hui, H., & Steinle-Neumann, G. (2015). Transport properties of silicate melts. *Rev. Geophys.*, *53*, 715–744. doi:10.1002/2015RG000485.

Nowacki, A., Wilks, M., Kendall, J.-M., Biggs, J., & Ayele, A. (2018). Characterising hydrothermal fluid pathways beneath Aluto volcano, Main Ethiopian Rift, using shear wave splitting. *J. Volcanol. Geotherm. Res.*, *356*, 331–341. doi:10.1016/j.jvolgeores.2018.03.023.

Parmigiani, A., Degruyter, W., Leclaire, S., Huber, C., & Bachmann, O. (2017). The mechanics of shallow magma reservoir outgassing. *Geochem. Geophys. Geosyst.*, *18*, 2887–2905. doi:10.1002/2017gc006912.

Pommier, A. (2014). Interpretation of magnetotelluric results using laboratory measurements. *Surv. Geophys.*, *35*, 41–84. doi:10.1007/s10712-013-9226-2.

Pommier, A., Gaillard, F., Pichavant, M., & Scaillet, B. (2008). Laboratory measurements of electrical conductivities of hydrous and dry Mount Vesuvius melts under pressure. *J. Geophys. Res. Solid Earth*, *113*. doi:10.1029/2007jb005269.

Quist, A. S., & Marshall, W. L. (1969). Electrical conductances of some alkali metal halides in aqueous solutions from 0 to 800. deg. and at pressures to 4000 bars. *The Journal of Physical Chemistry*, *73*, 978–985. doi:10.1021/j100724a037.

Rooney, T., Furman, T., Bastow, I., Ayalew, D., & Yirgu, G. (2007). Lithospheric modification during crustal extension in the Main Ethiopian Rift. *J. Geophys. Res. Solid Earth*, *112*. doi:10.1029/2006JB004916.

Rychert, C. A., Hammond, J. O., Harmon, N., Kendall, J. M., Keir, D., Ebinger, C., Bastow, I. D., Ayele, A., Belachew, M., & Stuart, G. (2012). Volcanism in the Afar Rift sustained by decompression melting with minimal plume influence. *Nat. Geosci.*, *5*, 406–409. doi:10.1038/ngeo1455.

Samrock, F., Grayver, A. V., Cherkose, B., Kuvshinov, A., & Saar, M. O. (2020). Aluto-Langano Geothermal Field, Ethiopia: Complete Image Of Underlying Magmatic-Hydrothermal System Revealed By Revised Interpretation Of Magnetotelluric Data. In *Proceedings World Geothermal Congress 2020*. Reykjavik, Iceland. doi:10.3929/ethz-b-000409980.

Samrock, F., Grayver, A. V., Eysteinsson, H., & Saar, M. O. (2018). Magnetotelluric image of transcrustal magmatic system beneath the Tulu Moye geothermal prospect in the Ethiopian Rift. *Geophys. Res. Lett.*, *45*, 12–847. doi:10.1029/2018GL080333.

Samrock, F., Kuvshinov, A., Bakker, J., Jackson, A., & Fisseha, S. (2015). 3-D analysis and interpretation of magnetotelluric data from the Aluto-Langano geothermal field, Ethiopia. *Geophys. J. Int.*, *202*, 1923–1948. doi:10.1093/gji/ggv270.

Trua, T., Deniel, C., & Mazzuoli, R. (1999). Crustal control in the genesis of Plio-Quaternary bimodal magmatism of the Main Ethiopian Rift (MER): geochemical and isotopic (Sr, Nd, Pb) evidence. *Chem. Geol.*, *155*, 201–231. doi:10.1016/s0009-2541(98)00174-0.

Tuffen, H., Smith, R., & Sammonds, P. R. (2008). Evidence for seismogenic fracture of silicic magma. *Nature*, *453*, 511–514. doi:10.1038/nature06989.

Wilks, M., Kendall, J.-M., Nowacki, A., Biggs, J., Wookey, J., Birhanu, Y., Ayele, A., & Bedada, T. (2017). Seismicity associated with magmatism, faulting and hydrothermal circulation at Aluto Volcano, Main Ethiopian Rift. *J. Volcanol. Geotherm. Res.*, *340*, 52–67. doi:10.1016/j.jvolgeores.2017.04.003.

Wilks, M., Rawlinson, N., Kendall, J.-M., Nowacki, A., Biggs, J., Ayele, A., & Wookey, J. (2020). The coupled magmatic and hydrothermal systems of the restless aluto caldera, ethiopia. *Frontiers in Earth Science*, *8*, 421. doi:10.3389/feart.2020.579699.

Wu, Y., Nakagawa, S., Kneafsey, T. J., Dafflon, B., & Hubbard, S. (2017). Electrical and seismic response of saline permafrost soil during freeze-thaw transition. *J. Appl. Geophys.*, *146*, 16–26. doi:10.1016/j.jappgeo.2017.08.008.

Yirgu, G., Ebinger, C., & Maguire, P. (2006). The Afar volcanic province within the East African Rift System. *Geological Society, London, Special Publications*, *259*, 1–6.